NANO LETTERS

pubs.acs.org/NanoLett Letter

Lorentz Force-Actuated Bidirectional Nanoelectromechanical Switch with an Ultralow Operation Voltage

Dianlun Li, Jiang Yan, Ying Zhang, Junzhuan Wang,* and Linwei Yu*

Cite This: *Nano Lett.* 2024, 24, 11403−11410 Read Online

ACCESS | Metrics & More | Article Recommendations | Supporting Information

ABSTRACT: The high operating voltage of conventional nanoelectromechanical switches, typically tens of volts, is much higher than the driving voltage of the complementary metal oxide semiconductor integrated circuit (~1 V). Though the operating voltage can be reduced by adopting a narrow air gap, down to several nanometers, this leads to formidable manufacturing challenges and occasionally irreversible switch failures due to the surface adhesive force. Here, we demonstrate a new nanowire-morphed nanoelectromechanical (NW-NEM) switch structure with ultralow operation voltages. In contrast to conventional nanoelectromechanical switches actuated by unidirectional electrostatic attraction, the NW-NEM switch is bidirectionally driven by Lorentz force to allow the use of a large air gap for excellent electrical isolation, while achieving a record-low driving voltage of <0.2 V. Furthermore, the introduction of the Lorentz force allows the NW-NEM switch to effectively overcome the adhesion force to recover to the turn-off state.

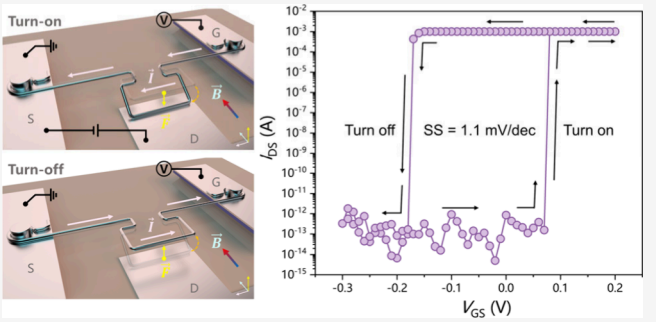

KEYWORDS: *nanoelectromechanical switch, Lorentz force actuation, ultralow operation voltage, silicon nanowire, in-plane solid−liquid−solid growth*

Electronic switching logic and memory units that can operate under harsh environments, such as intense radiative exposure and at high temperatures, are particularly important for nuclear emergency rescue, outer space missions, and critical industrial/battlefield operations.[1,2] This is because, as schematically depicted in Figure 1a, the conventional c-Si field effect transistor (FET) logic devices are prone to deteriorating or malfunctioning due to the radiation damage that accumulates in the gate dielectric[3,4] or to the thermal carrier breakdown happening at temperatures of >250 °C for c-Si logic devices.[5] In comparison, nanoelectromechanical (NEM) switches[6−12] rely on straightforward touching and detaching of electrodes to control the current flow and logic states, thus exempting the use of any dielectric layer and semiconducting channel materials. In this way, excellent switching performance can be accomplished, with a quasi-zero leakage current, an extremely steep subthreshold slope (SS), and an extremely high current on/off (I_{on}/I_{off}) ratio, even in high-temperature and hard radiation environments.[13−17]

Typical NEM switches were first constructed and tested within an in-plane configuration, as sketched in Figure 1b, which consists of a suspended conductive beam that can be attracted by lateral electrostatic force to bend and touch a nearby stationary electrode to turn on the current.[2,14,18,19] However, as the electrostatic force is inversely proportional to the square of the separation distance, $\sim 1/r^2$, a rather high operation voltage, typically of tens of volts, is usually required to effectively deform and/or bend the electrode beam, which is unavailable in conventional integrated circuits and also disadvantageous for power consumption and reliability controls.[14,20−27] To reduce the operation voltage (V_{op}) to <5 V, a narrow actuation air gap down to <30 nm[18] has to be used, which was fabricated with the aid of sophisticated deep ultraviolet (DUV) photolithography.[26,28] Another approach is to adopt an out-of-plane switch configuration,[13,20,24,29−31] which explores a sacrificial etching layer to achieve a narrow air gap of only 4 nm,[29] allowing thus a rather low operation voltage (V_{op}) of <1 V. However, this use of such a narrow air gap (g_{air}) also reduces significantly the mechanical restoring force of the electrode beam, typically scaling with $F_r \sim g_{air}$, and thus leads to new difficulty in easily and rapidly turning off the current. In fact, many of these narrow-gapped NEM switches become irreversible,[29,30,32−34] because the electrode beams (in the ON state) could be firmly attached and fixed by the prevalent adhesive forces at the touching interface. Though a trade-off can be sought by tuning the gap separation, a turn-on

Received: April 30, 2024
Revised: July 26, 2024
Accepted: July 29, 2024
Published: July 31, 2024

https://doi.org/10.1021/acs.nanolett.4c01999
Nano Lett. 2024, 24, 11403−11410

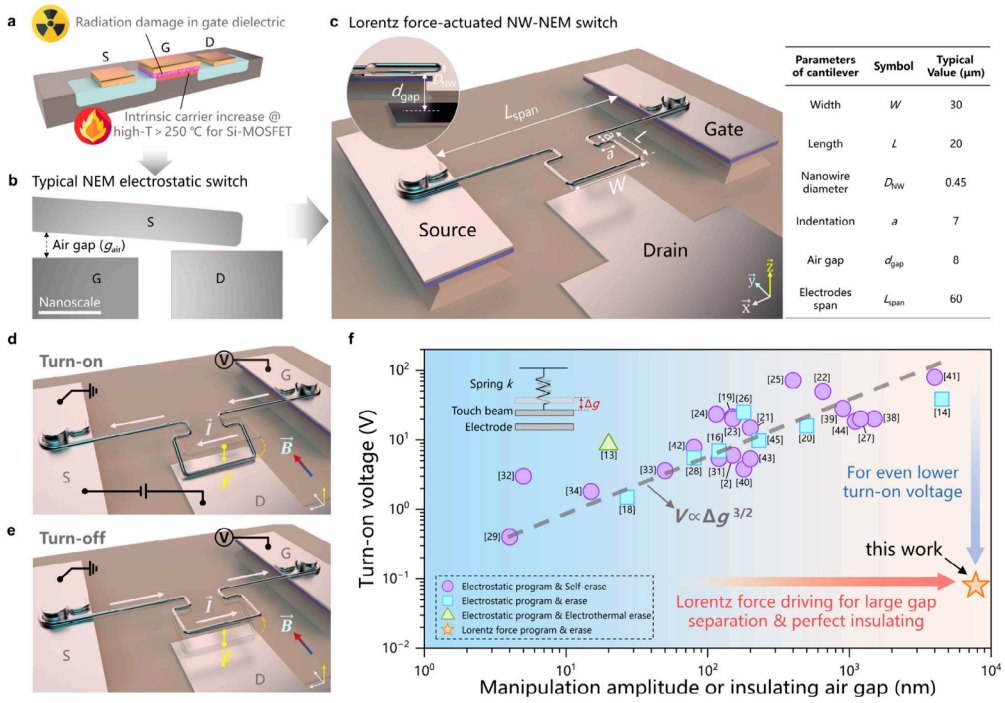

Figure 1. Design and operation principles of the nanowire-nanoelectromechanical (NW-NEM) switch. (a) Schematic of the fundamental structure of a conventional field effect transistor (FET), which will fail in harsh operation environments, such as exposure to intense radiation or high temperatures. In comparison, (b) the typical in-plane NEM switch, as reported in the literature, is usually driven by electrostatic attraction to enforce a beam electrode to travel over a narrow air gap, to touch or detach from the stationary electrode, for the ON or OFF state, respectively. (c) Schematic of the NW-NEM switch with a NW-cantilever and dimension information about the designed NW-NEM switch. (d) Schematic illustration of the turn-on operation. (e) Schematic illustration of the turn-off operation. (f) Comparison of the turn-on voltage vs the air gap (g_{air}) for NEM/MEM switch devices actuated by different methods, including electrostatic program and self-erase,[2,19,21−25,27,29,31−34,38−44] electrostatic program and erase,[14,16,18,20,26,28,45] electrostatic program and electrothermal erase,[13] and Lorentz force program and erase. The golden star represents the measured result of our NW-NEM switch in the magnetic field $|B_y| = 0.3$ T. The inset shows a schematic of the simplified lumped model for electrostatically actuated NEM/MEM switches. For electrostatically actuated devices, the turn-on voltage is roughly proportional to the $^3/_2$ power of the air gap.

voltage of 8.6 V is still needed, for example, for the NEM switch working with an optimized air gap of 20 nm.[13] Actually, this challenge can be better addressed if the driving force acting on the electrode beam can become bidirectional and thus drive the cantilever beam actively to approach or separate from the stationary electrodes, for the ON or OFF state, respectively, instead of the attraction-only and nonlinear electrostatic forces employed in all of the reported NEM switches.[2,13,29,31]

In this work, we propose a bidirectional NEM switch that is composed of a single suspended silicon nanowire (NW), grown via an in-plane solid−liquid−solid (IPSLS) approach,[35−37] with a protrusive cantilever as shown in Figure 1c. The slim NW arm actuated by the vectorial Lorentz force (LF) can be swiftly bent down to contact the bottom electrode (Figure 1d) or pulled out to overcome the van der Waals (vdW) force to turn off the circuit (Figure 1e). Note that the LF driving is bidirectional, linear, and independent of the air gap. Thus, a micrometer-scale air gap can be used here to guarantee perfect electric isolation, while achieving an ultralow operation voltage of <0.2 V, as marked in Figure 1f. This indicates that such a new NW-NEM switch design strategy can decouple the air gap from the required operating voltage as a beneficial capability for building high-performance NEMS logic devices operated at CMOS-level voltages.

As the key building blocks, the tailored ultrathin SiNW-cantilevers can be constructed in batches as orderly arrays via a step-edge-guided IPSLS approach.[46−48] Specifically, the planar SiNWs with the desired cantilever shape were first grown upon a patterned SiO_2/wafer substrate, by using indium (In) droplets as catalysts that absorb a precoated amorphous Si (a-Si) precursor layer to produce crystalline SiNWs. During this course, the In droplets can be attracted and guided by the prepatterned step edges to produce continuous SiNWs with a designable layout, as depicted schematically in Figure 2a. More experimental details of the IPSLS growth of SiNWs are available in the Methods or previous works.[37,49,50] Typical scanning electron microscopy (SEM) images of the as-grown NW-cantilever structure are presented in Figure S1. After the growth procedure, all of the remnant catalyst and unneeded NW portions were cleaned off via another masked etching (Figure 2b), preserving only the NW-cantilever portion of the desired line shape.

The as-grown NW-cantilevers were then picked up by using sharp fiber tips (Figure 2c and more details in the Supporting Information) and mounted upon a pair of standing pillars on the bottom isolated electrodes, with a diameter d_p of ∼10 μm and an electrode separation L_{span} of ∼60 μm, as shown in the optical microscope and SEM images shown in Figure 2e and its inset, respectively. To attach the NW-cantilever firmly upon the pillar electrode, a special hook-end design (Figure 2d,e) has been devised at the ends of the NWs. By setting a hook separation distance slightly shorter than $L_{hk} = L_{span} - \delta$, with δ1 μm, the NW-cantilever can be firmly self-locked upon the

https://doi.org/10.1021/acs.nanolett.4c01999
Nano Lett. 2024, 24, 11403−11410

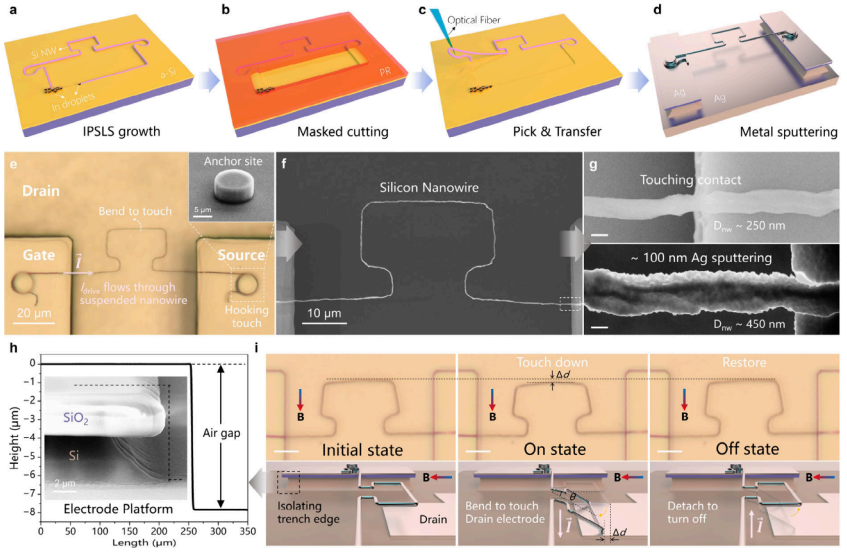

Figure 2. Device fabrication and NEM switching. (a) Guided growth formation of tailored ultralong SiNWs, with desired switch shapes, via an IPSLS mechanism led by indium (In) droplets consuming a-Si precursor layer coated on the surface, followed by (b) the etching of unneeded SiNW portions by using the photoresist as a mask, leaving only the cantilever part. (c and d) Pick-and-place transferring of the tailored SiNWs, mounted onto a pair of bottom-isolated electrode platforms, prior to deposition of a silver (Ag) layer to form conductive Ag/Si NWs, suspended and fixed at a pair of standing pillar electrodes. (e and f) Top-view optical and SEM images, respectively, of a suspended SiNW-cantilever, self-locked upon the pillar electrodes. (g) Enlarged SEM views of the SiNW contact to the platform edge, before and after Ag sputtering. The scale bar is 200 nm. (h) Height profile of the bottom-isolated electrode platform measured by a profilometer, with a side-view SEM image of the platform edge shown in the inset. (i) Optical images of the initial, ON, and OFF states of the NW switch, from left to right, respectively, with scale bars representing 10 μm.

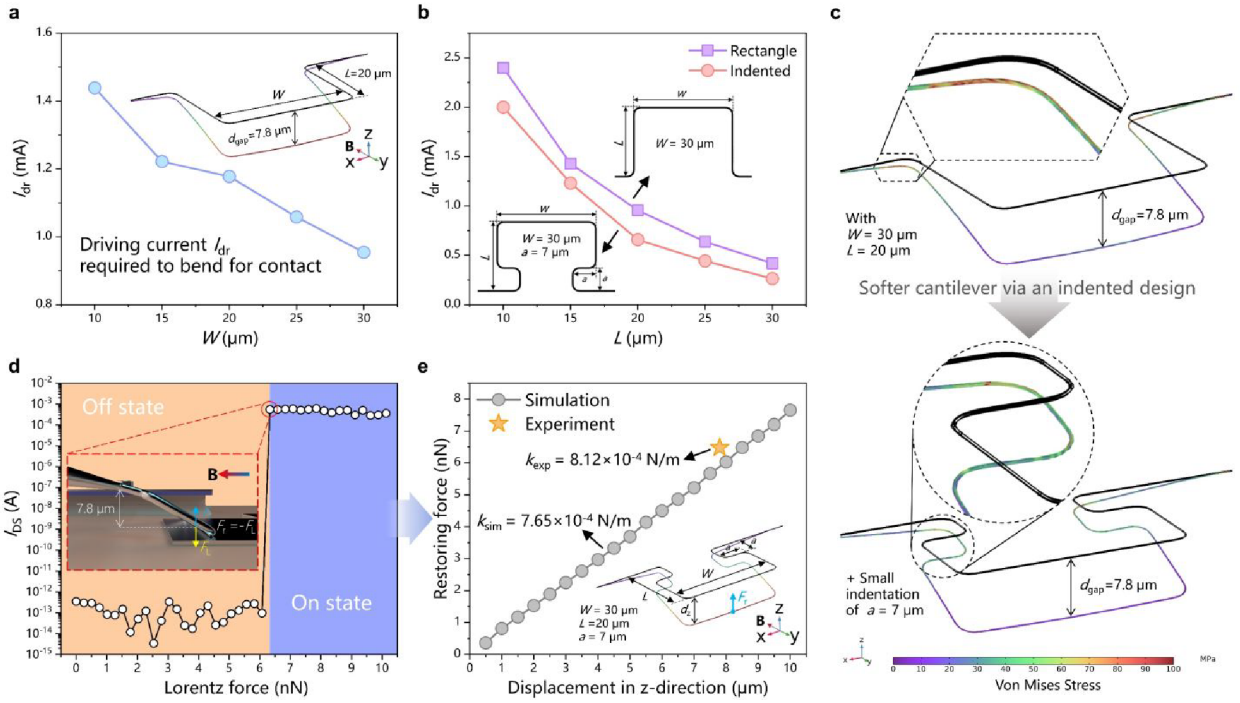

Figure 3. Structural design and analysis of the NW-NEM switch. (a) Simulated driving current I_{dr} required to bend for contact with respect to width W of the rectangular NW-cantilever (length L = 20 μm; air gap d_{gap} = 7.8 μm). (b) Comparison of simulated driving current−length (I_{dr}−L) curves between the rectangle and indented NW-cantilever. (c) FEM simulation of Von Mises stress in the rectangle (top) and indented (bottom) NW-cantilever. (d) I_{DS}−F_L characteristics of the NW-NEM switch with an indented cantilever. The inset shows the schematic of the transient force analysis of the NW-cantilever touch drain electrode. (e) Simulated restoring force with respect to the displacement in the z-direction (d_z). The golden star represents the experimental result for the NW-NEM switch.

standing pillars. Then, a ∼100 nm thick silver (Ag) layer was evaporated by using magnetron sputtering to form a highly conductive and suspended Ag/SiNW bridge pathway connecting the two bottom-isolated platforms, as shown, for example, in panels f and g of Figure 2, with a typical resistance (R_{NW}) of ∼230 Ω. Here, the switch air gap, that is, the separation

https://doi.org/10.1021/acs.nanolett.4c01999
Nano Lett. 2024, 24, 11403−11410

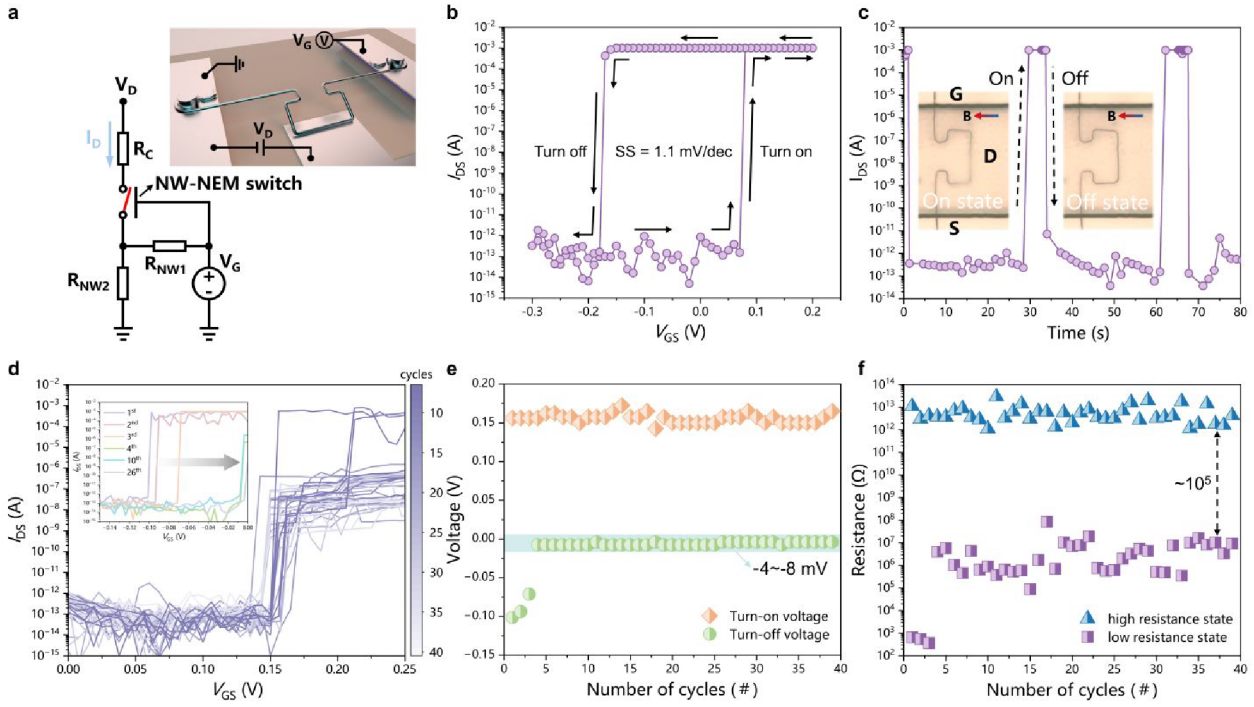

Figure 4. Switch operation characteristics. (a) Schematic of the equivalent circuit of the NW-NEM switch. (b) $I_{DS}-V_{GS}$ dual-sweep characteristics of the fabricated NW-NEM switch at a V_{DS} of 0.3 V, where the transport current increases abruptly at an applied voltage of 80 mV (which increased quickly to a compliance current of 1 mA) and decreases at a gating voltage of −180 mV. (c) Dynamic switching responses of the NW-NEM switch recorded at a V_{DS} of 0.3 V. (d) $I_{DS}-V_{GS}$ characteristics at a V_{DS} of 0.3 V during cyclic measurements. (e) Turn-on and turn-off voltage evolution curves with an increase in the number of cycles. (f) Variations of the low-resistance state (LRS) at the ON state and the high-resistance state (HRS) at the OFF state with the number of switching cycles.

between the suspended NW-cantilever and the bottom electrode, is set by the heights of the platforms, which is ∼7.8 μm (H_{gap}), as shown in the side-view SEM image presented in Figure 2h and confirmed by step profiler measurement. More fabrication details of the platform and pillar structures are explained in Figure S2.

The mechanical behavior of the NW-cantilever was optically evaluated. Figure 2i presents the top-view microscope images of the typical as-fabricated NW-cantilever at the initial, ON, and OFF states. This switching operation was carried out within a constant lateral $|B_y|$ = 0.3 T, passing an electric bias voltage of 0.2 V to enforce the cantilever to bend and touch down the bottom electrode, as inferred from the middle panel optical image in Figure 2i, which reveals a slight defocus of the NW-cantilever end, with a horizontal displacement Δd of ∼1.2 μm, corresponding to an estimated bending angle θ of ∼20°. Upon touching the bottom electrode pad surface, the NW-cantilever was fixed at the ON state by the adhesive force, even when the drive voltage was removed, indicating a stable nonvolatile switching behavior. To switch off, an opposite drive voltage of −0.2 V was applied, causing an upward-lifting LF to pull back the NW-cantilever and recover to the initial OFF state. Compared to the attractive only electrostatic force (EF) driving widely used in the NEM switches,[2,21] the LF driving here is bidirectional and thus can help to counter the adhesive interfacial force.

For the simplest form of a rectangle-shaped cantilever (inset of Figure 3a), with a protrusive arm that measures L in extension and W in width, a FEM simulation was first carried out. The structural deformation under LF driving was predicted, and minimal driving current I_{dr} required for the cantilever with a different geometry design to turn on the contact was extracted. For example, with a constant lateral extension L of 20 μm, Figure 3a plots minimal drive current I_{dr} against varied arm width W. The FEM simulation results indicate that the required drive current can be readily reduced, by 34%, by adopting a wider arm width, due to the increase in LF torque force around the x-axis, that is roughly

$$T = F_{LF}L = IB_yWL = IB_yS_{ct} \quad (1)$$

where S_{ct} is the effective arm area encircled by the NW-cantilever.

Though a larger torque force can be obtained by increasing L or W, it always comes with an increased device area and thus a reduced integration density as well as unfavorable cantilever structure stability under gravity dragging. Therefore, in pursuit of an even lower drive current within the same cantilever area, a more flexible indented cantilever design (as shown in the bottom left inset of Figure 3b) has been introduced to reduce the stiffness of the suspended electrode arm and facilitate the downward touching turn-on operation. Figure 3b presents and compares the I_{dr} evolutions for the rectangular and indented arm cantilevers, with a constant width W of 30 μm and an indented size a of 7 μm, against different extension lengths L. One can see that the indented arm structure can indeed help to reduce the driving current required for effective turn-on switching. To better understand the advantages of this design, FEM simulations presented in Figure 3c reveal more details of the Von Mises stress distributions along these two different cantilever structures with the same W and L. It is found that to reach the same deflection under LF driving to touch the bottom electrode, the maximum stress induced within the indented NW-cantilever is located at the turning corners of ∼52 MPa, far below the yield stress of the Si NW (∼500 MPa

https://doi.org/10.1021/acs.nanolett.4c01999
Nano Lett. 2024, 24, 11403−11410

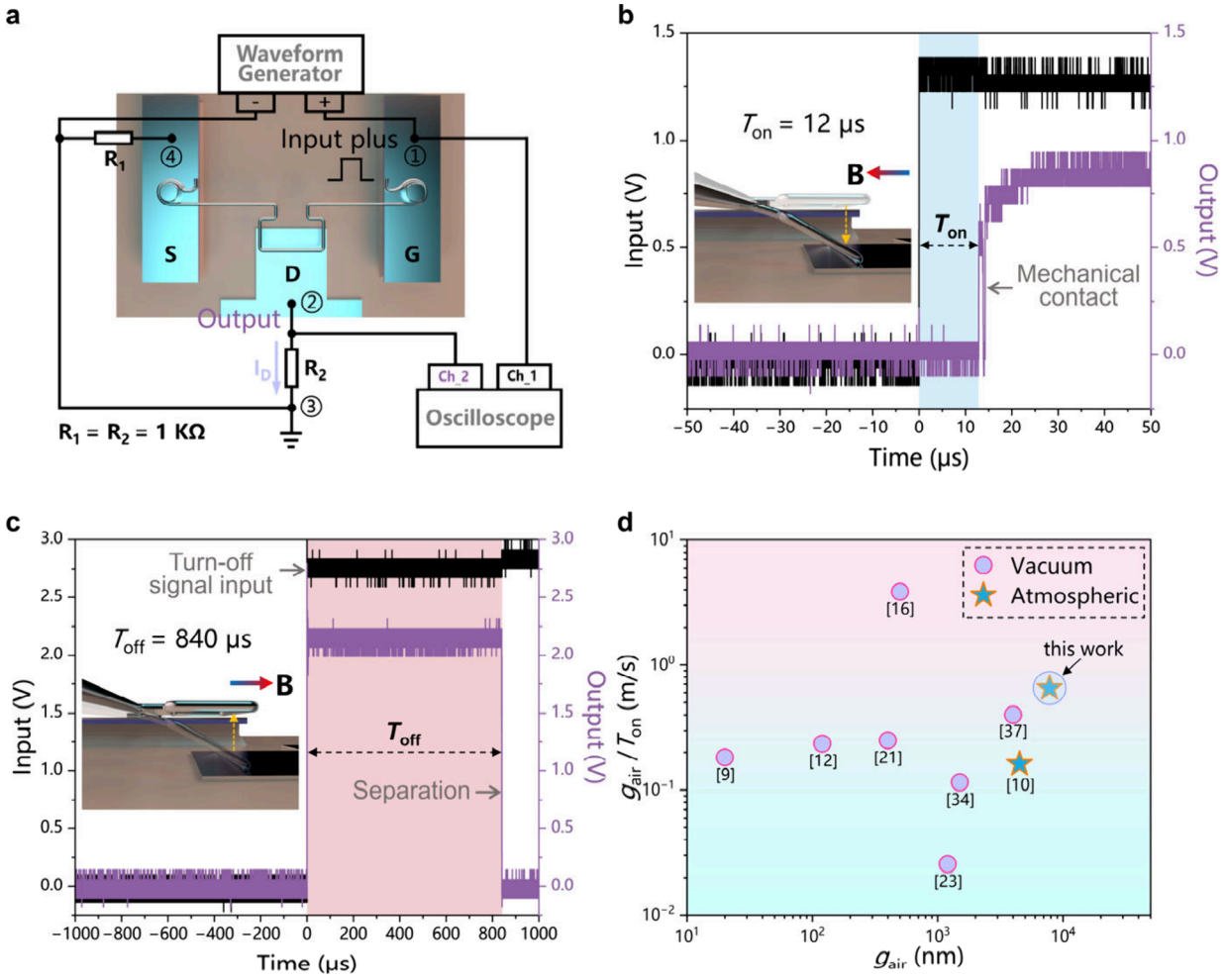

Figure 5. Dynamic response and delay times. (a) Experimental setup and circuit configuration for the evaluation of dynamic responses of the NW-based NEM switch. (b and c) Mechanical transient responses for the on and off switching operations, respectively. (d) Comparison of the turn-on speed (defined as the ratio of the air gap to the turn-on delay time) vs g_{air} for the NEM/MEM switch devices measured in vacuum (circle) and in an atmosphere (star) in the literature.

to 12 GPa)[51,52] and also much lower than that at the root of the rectangular NW-cantilever (~88 MPa). This indicates that flexible line-shape engineering of the NW-cantilever plays a critical role in the resulting the stable mechanical deformation and elastic response. Finally, the dimension parameters of the optimally designed NW-NEM switch are shown in Figure 1c.

For the NW-NEM switch to behave in a nonvolatile manner in the turn-on operation, the adhesive force should be larger than the restoring force of the deflected cantilever, $F_{adh} > F_r \sim d_{gap}k$, where k is the stiffness of the NW-cantilever. The stiffness is estimated by FEM simulation to be 7.65×10^{-4} N/m (Figure 3e), quite close to the experimental value of 8.12×10^{-4} N/m as extracted by monitoring the current (I_{DS}) switching during a turn-on operation, as shown in Figure 3d. Note that, though the exact value of the adhesive force (vdW force) is unknown (see Supplementary Note 1), the mechanical stiffness of the cantilever structure can be readily adjusted to achieve such a nonvolatile ON state, by changing the setting of the W and L parameters.

In Figure 4a, an equivalent electric circuit is presented for the switching operation of the NW-NEM switch. The NW-cantilever can be separated into two segments at the middle touching point, with corresponding resistances of R_{NW1} and R_{NW2}, while there is another serial contact resistance (R_C) between the NW-cantilever and the drain electrode. The devices were operated within a constant magnetic field of B_y = 0.3 T. Figure 4b shows the typical $I_{DS}-V_G$ dual-sweep characteristics of the NW-NEM switch at a V_{DS} of 0.3 V. Note that to protect the switch circuit, the ON state current was limited to 1 mA. Specifically, when the gate voltage swept from a V_{GS} of <0 at the initial OFF state to 80 mV, the I_{DS} current was quickly turned on and increased from below I_{off} = 10^{-13} A to the saturation current, over more than 10 orders of magnitude, achieving an extremely high current ON/OFF ratio of $>10^{10}$, and a subthreshold swing (SS) of only 1.1 mV decade^{-1}. Then, a similar abrupt current drop was also observed in the backward scan but at a reversed gate voltage V_{GS} of −0.18 V, indicating that the adhesive force at the touched electrodes was strong enough to keep the cantilever to stay in this ON state, until an inverse LF was applied to detach them at a V_{GS} of −0.18 V. A close view of this NW-cantilever switching behavior in the ON and OFF states is provided in the insets of Figure 4c, while the switch was toggled between the ON and OFF states controlled by a sequence of gate voltage alternation between V_{GS} values of 0.2 and −0.2 V, under a constant V_{DS} of 0.3 V, as shown in Figure 4c.

Figure 4d and its inset present the evolution of the turn-on and turn-off $I_{DS}-V_{GS}$ curves during the initial 39 cyclic

https://doi.org/10.1021/acs.nanolett.4c01999
Nano Lett. 2024, 24, 11403−11410

Table 1. Comparison of the NW-Cantilever Switch to the NEM Switches in the Literature

electrode configuration	operating mechanisms	air gap	fabrication method	turn-on voltage (V)	turn-off voltage (V)	mechanical delay	on/off ratio	endurance	ref
in-plane	electrostatic program and erase	120 nm	electron beam lithography	>7	>8	511 ns (simulated)	~10^3	42 cycles (nonvolatility)	16
in-plane	electrostatic program and erase	80 nm	BEOL CMOS manufacturing processes (16 nm node)	5.5	7.5		~10^4	>3 cycles (nonvolatility)	28
in-plane	electrostatic program and erase	4.5 μm	laser machining	38.5	40.5	28 μs	~10^6	10^6 cycles (volatility)	14
out-of-plane	electrostatic program	4 nm	self-aligned trench formation	0.4			~10^5	<20 cycles (nonvolatility)	29
out-of-plane	electrostatic program and erase	500 nm	electron beam lithography	16	16	130 ns	~10^4	500 cycles (volatility)	20
out-of-plane	electrostatic program and electrothermal erase	20 nm	KrF scanner	>8.6	0.9	110 ns	~10^3	23 cycles (nonvolatility)	13
out-of-plane	Lorentz force program and erase	7.8 μm	growth of IPSLS SiNWs and suspend	<0.16	<0.11	12 μs	~10^{10}	10^4 cycles (nonvolatility)	this work

measurements. It is found that the turn-on transitions usually happened at relatively more stable voltages, ranging from 0.13 to 0.17 V, indicating the excellent mechanical stability of the suspended NW-cantilever. Similar turn-on voltages are also demonstrated in three extra devices, as shown in Figure S3. In comparison, though an inverse LF driving can steadily pull back the electrode to turn off the current, the turn-off voltage gradually shifts from 100 to <10 mV during its first 10 switching-off operations. Alternatively, the measured curves in Figure 4d occasionally demonstrate an interesting switching behavior with stepwise increases in current, and more details are discussed in Figure S4. As shown in panels e and f of Figure 4, the turn-on and turn-off operations become stable after the initial approximately four cycles in terms of both the switching voltages and the ratio of the high- and low-resistance states. The initial turn-off voltage shifting is accompanied by an increase in the contact resistance, as witnessed from the fourth turn-off curve, where the channel current decreased from 10^{-3} to 10^{-7} A. Note that similar current fluctuations were also observed for the turn-on operations. This current decrease could be ascribed to the modification of contact conditions at the electrode touching points, after experiencing the initial mechanical impact and passing current stress, which usually leads to a reduced contact surface area, mechanical abrasion, or even material transfer. Though the exact mechanism remains unclear, there have been reports about the improvement of the electrical contacts for NEM switches by using a more stable and wear-resistant coating layer of Pt,[14] graphene,[31] CNT,[53] and alloys,[54] which could help to improve the electric stability and reliability of the NW-cantilever contact interfaces. To further test its mechanical reliability, the NW-NEM switch was turned on and off for 10 000 cycles, as shown in the $I_{DS}-V_{GS}$ curves in panels a and b of Figure S5. The nonvolatile switching operation was stably maintained for 10 000 cycles, which is 250 times the endurance of recently reported nonvolatile NEM switches.[13,16] Because of to the rather soft NW-cantilever design and efficient Lorentz force-driving scheme, the NW-NEM switch can operate steadily at rather low operating voltages without mechanical buckling or snapping failures. However, the increased turn-on voltages during endurance tests need to be improved. The problem can be caused by the increased resistance of the NW-cantilever, as shown in Figure S5c.

Transient switching responses of the NW-NEM switch were characterized in a setup, as diagrammed in Figure 5a. Specifically, the voltage built up over the load resistor R_2 was monitored for the turn-on state between the source and drain electrodes, while resistor R_1 is used to stabilize the current between the source and gate electrodes. All of the experiments were carried out under atmospheric conditions. As shown in panels b and c of Figure 5, the turn-on and turn-off delay times of a NW-NEM switch were determined to be 12 and 840 μs, respectively. For the turn-off operation, even with the active LF pulling out, the detachment of the contacted NW-cantilever seems to be delayed by the larger contact adhesive force due to the higher contact velocity at turn-on operation.[28] According to the analytical model of the turn-off time (see Supplementary Note 2), the turn-off time will increase with the mass and the resistance of the NW-cantilever as well as the actual strength of the vdW force at the contact interface. Also, a stiffer cantilever, a stronger background magnetic field, and a larger applied pull-out voltage/current will ensure a faster turn-off operation. Finally, we benchmarked the turn-on speed of this NW-cantilever switch with those reported in the literature and present it in Figure 5d, where the turn-on speed is defined as the ratio of the air gap separation to the turn-on delay time. As we can see, even compared to most of the NEM switches operated in a vacuum, the NW-cantilever switch achieves a rather high turn-on speed with the largest air gap under atmospheric conditions. This is indeed an encouraging debut for the Lorentz force-actuated switch devices, as it is expected that the NW-NEM will operate faster under similar vacuum conditions, while the successful atmospheric demonstration is also closer to a practical application environment.

In summary, we have demonstrated a bidirectional Lorentz force (LF)-actuated NEM switch, with a unique flexible cantilever design, formed by individual ultralong Si nanowires grown via the IPSLS approach. Table 1 presents a more comprehensive comparison of this NW-cantilever NEM switch to the recently reported NEM/MEM switches. Our NW-cantilever switch can operate at a rather low driving voltage, <0.2 V, which is 1−2 orders of magnitude lower than the reported operating voltages of typical electrostatically driven NEM switches. More importantly, this bidirectional LF-driving scheme allows for the use of micrometer-scale large air gaps to achieve perfect electric isolation, while providing a feasible solution to resolve the notorious adhesion problem at the

https://doi.org/10.1021/acs.nanolett.4c01999
Nano Lett. 2024, 24, 11403−11410

touched cantilever/electrode interface that usually leads to irreversible switching failure from the ON to OFF states. These capabilities combined enable a swift on/off switching, a large current on/off ratio of $>10^{10}$, and an excellent subthreshold swing down to 1.1 mV decade^{-1}. These results highlight the potential of the NW-cantilever structure in the development of a new generation of integratable NEM switch logic, memory, and sensor units for harsh environmental operations. Moreover, in view of further size miniaturization for a higher integration density, the footprint of the NW-cantilevers can be readily scaled down in size by at least 20-fold, as shown for example in Figure S6. In fact, the diameter of the IPSLS SiNWs can be readily controlled to <20 nm,[55] leaving plenty of room for the formation of smaller and more delicate cantilever arms, catering to specific needs in functional design. Also, the suspension of the NW can be accomplished via selective dry etching of the targeted underlying regions. Therefore, one can envision that the high-density integration of such NW-NEM switches is technically feasible and will advance the development of NEM electronics requiring a high device density and large-area processability.

■ ASSOCIATED CONTENT

Data Availability Statement

All data are available in the main text or the Supporting Information.

Supporting Information

The Supporting Information is available free of charge at https://pubs.acs.org/doi/10.1021/acs.nanolett.4c01999.

Methods, typical SEM image of the as-grown SiNW-cantilever, fabrication of the electrode platforms with anchor pillars, device-to-device variability of NW-NEM switches, stepped switching behavior of the NW-NEM switch, cyclic measurements of the NW-NEM switch, miniaturization demonstration of the NW-NEM switch, analysis of the van der Waals force between contact surfaces, and mathematical modeling of the turn-on voltage and turn-on and turn-off times (PDF)

■ AUTHOR INFORMATION

Corresponding Authors

Junzhuan Wang − *School of Electronic Science and Engineering, National Laboratory of Solid-State Microstructures, Nanjing University, 210023 Nanjing, China*; Email: wangjz@nju.edu.cn

Linwei Yu − *School of Electronic Science and Engineering, National Laboratory of Solid-State Microstructures, Nanjing University, 210023 Nanjing, China*; orcid.org/0000-0002-0801-5210; Email: yulinwei@nju.edu.cn

Authors

Dianlun Li − *School of Electronic Science and Engineering, National Laboratory of Solid-State Microstructures, Nanjing University, 210023 Nanjing, China*; orcid.org/0000-0003-0073-9457

Jiang Yan − *School of Electronic Science and Engineering, National Laboratory of Solid-State Microstructures, Nanjing University, 210023 Nanjing, China*; orcid.org/0000-0002-6079-5058

Ying Zhang − *School of Electronic Science and Engineering, National Laboratory of Solid-State Microstructures, Nanjing University, 210023 Nanjing, China*

Complete contact information is available at: https://pubs.acs.org/10.1021/acs.nanolett.4c01999

Author Contributions

D.L. and J.Y. contributed equally to this work. Conceptualization: L.Y. and D.L. Methodology and analysis: D.L., J.Y., Y.Z., J.W., and L.Y. Investigation: D.L., J.Y., and L.Y. Funding acquisition: L.Y. and J.W. Visualization: D.L. and L.Y. Supervision: J.W. and L.Y. Writing of the original draft: D.L. and L.Y. Review and editing: D.L., J.Y., Y.Z., J.W., and L.Y.

Notes

The authors declare no competing financial interest.

■ ACKNOWLEDGMENTS

This work was supported by the National Key Research Program of China (92164201), the National Natural Science Foundation of China for Distinguished Young Scholars (62325403), and the National Natural Science Foundation of China (61934004).

■ REFERENCES

(1) Prinzie, J.; Simanjuntak, F. M.; Leroux, P.; Prodromakis, T. Low-power electronic technologies for harsh radiation environments. *Nature Electronics* **2021**, *4*, 243−253.

(2) Lee, T.-H.; Bhunia, S.; Mehregany, M. Electromechanical Computing at 500°C with Silicon Carbide. *Science* **2010**, *329*, 1316−1318.

(3) Zhu, M.; et al. Radiation-hardened and repairable integrated circuits based on carbon nanotube transistors with ion gel gates. *Nature Electronics* **2020**, *3*, 622−629.

(4) Fang, R.; et al. Total ionizing dose effect of γ-ray radiation on the switching characteristics and filament stability of HfOx resistive random access memory. *Appl. Phys. Lett.* **2014**, *104*, 183507.

(5) Neudeck, P. G.; Okojie, R. S.; Chen, L.-Y. High-temperature electronics - a role for wide bandgap semiconductors? *Proc. IEEE* **2002**, *90*, 1065−1076.

(6) Loh, O. Y.; Espinosa, H. D. Nanoelectromechanical contact switches. *Nat. Nanotechnol.* **2012**, *7*, 283−295.

(7) Kim, C.; Marsland, R.; Blick, R. H. The Nanomechanical Bit. *Small* **2020**, *16*, 2001580.

(8) Feng, P. X. L. NEMS switches: Opportunities and challenges in emerging IC technologies. In *2015 International Conference on IC Design & Technology (ICICDT)*; 2015.

(9) Siahlo, A. I.; Popov, A. M.; Poklonski, N. A.; Lozovik, Y. E.; Vyrko, S. A. Graphene membrane-based NEMS for study of interface interaction. *Physica E: Low-dimensional Systems and Nanostructures* **2020**, *115*, 113645.

(10) Chaudhary, R.; Mudimela, P. R. 3D modeling of graphene oxide based nanoelectromechanical capacitive switch. *Microsystem Technologies* **2020**, *26*, 2931−2937.

(11) Chaudhary, R.; Jhanwar, P.; Mudimela, P. R. Finite Element Analysis of Graphene Oxide Hinge Structure-based RF NEM Switch. *IETE Journal of Research* **2023**, *69*, 967−974.

(12) Mayet, A. M.; Muqeet, M. A.; Alhashim, H. H.; Kurdahi, F.; Eftekhari-Zadeh, E. Sub-0.3 V amorphous metal WNx based NEMS switch with 8 trillion cycles. *Front. Mater.* **2024**, *10*, 1337925.

(13) Lee, Y.-B.; et al. Sub-10 fJ/bit radiation-hard nanoelectromechanical non-volatile memory. *Nat. Commun.* **2023**, *14*, 460.

(14) Jo, E.; Kang, Y.; Sim, S.; Lee, H.; Kim, J. High-Temperature-Operable Electromechanical Computing Units Enabled by Aligned Carbon Nanotube Arrays. *ACS Nano* **2023**, *17*, 13310−13318.

(15) Hwang, K.-M.; et al. Nano-electromechanical Switch Based on a Physical Unclonable Function for Highly Robust and Stable Performance in Harsh Environments. *ACS Nano* **2017**, *11*, 12547−12552.

(16) Rana, S.; et al. Nanoelectromechanical relay without pull-in instability for high-temperature non-volatile memory. *Nat. Commun.* **2020**, *11*, 1181.
(17) Choi, J.; Lee, J.-I.; Eun, Y.; Kim, M.-O.; Kim, J. Aligned Carbon Nanotube Arrays for Degradation-Resistant, Intimate Contact in Micromechanical Devices. *Adv. Mater.* **2011**, *23*, 2231−2236.
(18) Feng, X. L.; Matheny, M. H.; Zorman, C. A.; Mehregany, M.; Roukes, M. L. Low Voltage Nanoelectromechanical Switches Based on Silicon Carbide Nanowires. *Nano Lett.* **2010**, *10*, 2891−2896.
(19) Qian, Y.; Soon, B. W.; Singh, P.; Campanella, H.; Lee, C. All metal nanoelectromechanical switch working at 300 °C for rugged electronics applications. *Nanoscale* **2014**, *6*, 5606−5611.
(20) Lee, S. W.; Park, S. J.; Campbell, E. E. B.; Park, Y. W. A fast and low-power microelectromechanical system-based non-volatile memory device. *Nat. Commun.* **2011**, *2*, 220.
(21) Jang, J. E.; et al. Nanoscale memory cell based on a nanoelectromechanical switched capacitor. *Nat. Nanotechnol.* **2008**, *3*, 26−30.
(22) Hayamizu, Y.; et al. Integrated three-dimensional microelectromechanical devices from processable carbon nanotube wafers. *Nat. Nanotechnol.* **2008**, *3*, 289−294.
(23) Lee, S. W.; et al. A Three-Terminal Carbon Nanorelay. *Nano Lett.* **2004**, *4*, 2027−2030.
(24) Loh, O.; Wei, X.; Sullivan, J.; Ocola, L. E.; Divan, R.; Espinosa, H. D. Carbon-Carbon Contacts for Robust Nanoelectromechanical Switches. *Adv. Mater.* **2012**, *24*, 2463−2468.
(25) Jo, E.; et al. Integration of a Carbon Nanotube Network on a Microelectromechanical Switch for Ultralong Contact Lifetime. *ACS Appl. Mater. Interfaces* **2019**, *11*, 18617−18625.
(26) Sikder, U.; Tatum, L. P.; Yen, T. T.; Liu, T. J. K. Vertical NV-NEM Switches in CMOS Back-End-of-Line: First Experimental Demonstration and Array Programming Scheme. In *2020 IEEE International Electron Devices Meeting (IEDM)*; 2020.
(27) Chung, S.; Ul Karim, M. A.; Kwon, H.-J.; Subramanian, V. High-Performance Inkjet-Printed Four-Terminal Microelectromechanical Relays and Inverters. *Nano Lett.* **2015**, *15*, 3261−3266.
(28) Sikder, U.; Naous, R.; Stojanović, V.; Liu, T. J. K. Non-Volatile Nano-Electro-Mechanical Switches and Hybrid Circuits in a 16 nm CMOS Back-End-of-Line Process. *IEEE Electron Device Lett.* **2023**, *44*, 136−139.
(29) Lee, J. O.; et al. A sub-1-V nanoelectromechanical switching device. *Nat. Nanotechnol.* **2013**, *8*, 36−40.
(30) Lee, J. O.; et al. Nanomechanical Encoding Method Using Enhanced Thermal Concentration on a Metallic Nanobridge. *ACS Nano* **2017**, *11*, 7781−7789.
(31) Liu, X.; et al. Large Arrays and Properties of 3-Terminal Graphene Nanoelectromechanical Switches. *Adv. Mater.* **2014**, *26*, 1571−1576.
(32) Dujardin, E.; Derycke, V.; Goffman, M. F.; Lefèvre, R.; Bourgoin, J. P. Self-assembled switches based on electroactuated multiwalled nanotubes. *Appl. Phys. Lett.* **2005**, *87*, 193107.
(33) Cha, S. N.; et al. Fabrication of a nanoelectromechanical switch using a suspended carbon nanotube. *Appl. Phys. Lett.* **2005**, *86*, 083105.
(34) Subramanian, A.; Dong, L. X.; Nelson, B. J.; Ferreira, A. Supermolecular switches based on multiwalled carbon nanotubes. *Appl. Phys. Lett.* **2010**, *96*, 073116.
(35) Yu, L.; Alet, P.-J.; Picardi, G.; Roca i Cabarrocas, P. An In-Plane Solid-Liquid-Solid Growth Mode for Self-Avoiding Lateral Silicon Nanowires. *Phys. Rev. Lett.* **2009**, *102*, 125501.
(36) Sun, Y.; Dong, T.; Yu, L.; Xu, J.; Chen, K. Planar Growth, Integration, and Applications of Semiconducting Nanowires. *Adv. Mater.* **2020**, *32*, 1903945.
(37) Yan, J.; Zhang, Y.; Liu, Z.; Wang, J.; Xu, J.; Yu, L. Ultracompact single-nanowire-morphed grippers driven by vectorial Lorentz forces for dexterous robotic manipulations. *Nat. Commun.* **2023**, *14*, 3786.
(38) Soon, B. W.; et al. Fabrication and Characterization of a Vacuum Encapsulated Curved Beam Switch for Harsh Environment Application. *Journal of Microelectromechanical Systems* **2014**, *23*, 1121−1130.
(39) Ke, C.; Espinosa, H. D. In Situ Electron Microscopy Electromechanical Characterization of a Bistable NEMS Device. *Small* **2006**, *2*, 1484−1489.
(40) Sun, J.; Muruganathan, M.; Kanetake, N.; Mizuta, H. Locally-Actuated Graphene-Based Nano-Electro-Mechanical Switch. *Micromachines* **2016**, *7*, 124−130.
(41) Seo, M.-H.; et al. >1000-Fold Lifetime Extension of a Nickel Electromechanical Contact Device via Graphene. *ACS Appl. Mater. Interfaces* **2018**, *10*, 9085−9093.
(42) Huynh Van, N.; Muruganathan, M.; Kulothungan, J.; Mizuta, H. Fabrication of a three-terminal graphene nanoelectromechanical switch using two-dimensional materials. *Nanoscale* **2018**, *10*, 12349−12355.
(43) Kam, H.; Pott, V.; Nathanael, R.; Jaeseok, J.; Elad, A.; Tsu-Jae King, L. Design and reliability of a micro-relay technology for zero-standby-power digital logic applications. In *2009 IEEE International Electron Devices Meeting (IEDM)*; 2009.
(44) Rana, S.; et al. Nano-crystalline graphite for reliability improvement in MEM relay contacts. *Carbon* **2018**, *133*, 193−199.
(45) Sikder, U.; et al. Toward Monolithically Integrated Hybrid CMOS-NEM Circuits. *IEEE Trans. Electron Devices* **2021**, *68*, 6430−6436.
(46) Yu, L.; Oudwan, M.; Moustapha, O.; Fortuna, F.; Roca i Cabarrocas, P. Guided growth of in-plane silicon nanowires. *Appl. Phys. Lett.* **2009**, *95*, 113106.
(47) Xue, Z.; et al. Deterministic Line-Shape Programming of Silicon Nanowires for Extremely Stretchable Springs and Electronics. *Nano Lett.* **2017**, *17*, 7638−7646.
(48) Hu, R.; et al. Unprecedented Uniform 3D Growth Integration of 10-Layer Stacked Si Nanowires on Tightly Confined Sidewall Grooves. *Nano Lett.* **2020**, *20*, 7489−7497.
(49) Liu, Z.; et al. Ab Initio Design, Shaping, and Assembly of Free-Standing Silicon Nanoprobes. *Nano Lett.* **2021**, *21*, 2773−2779.
(50) Dong, T.; et al. Monolithic Integration of Silicon Nanowire Networks as a Soft Wafer for Highly Stretchable and Transparent Electronics. *Nano Lett.* **2019**, *19*, 6235−6243.
(51) Zhu, Y.; Xu, F.; Qin, Q.; Fung, W. Y.; Lu, W. Mechanical Properties of Vapor−Liquid−Solid Synthesized Silicon Nanowires. *Nano Lett.* **2009**, *9*, 3934−3939.
(52) Hoffmann, S.; et al. Measurement of the Bending Strength of Vapor−Liquid−Solid Grown Silicon Nanowires. *Nano Lett.* **2006**, *6*, 622−625.
(53) Lee, J. I.; Song, Y.; Jung, H.; Choi, J.; Eun, Y.; Kim, J. Deformable Carbon Nanotube-Contact Pads for Inertial Microswitch to Extend Contact Time. *IEEE Transactions on Industrial Electronics* **2012**, *59*, 4914−4920.
(54) Sim, G.-D.; et al. Nanotwinned metal MEMS films with unprecedented strength and stability. *Sci. Adv.* **2017**, *3*, No. e1700685.
(55) Hu, R.; et al. Ultra-Confined Catalytic Growth Integration of Sub-10 nm 3D Stacked Silicon Nanowires Via a Self-Delimited Droplet Formation Strategy. *Small* **2022**, *18*, 2204390.

https://doi.org/10.1021/acs.nanolett.4c01999
Nano Lett. 2024, 24, 11403−11410